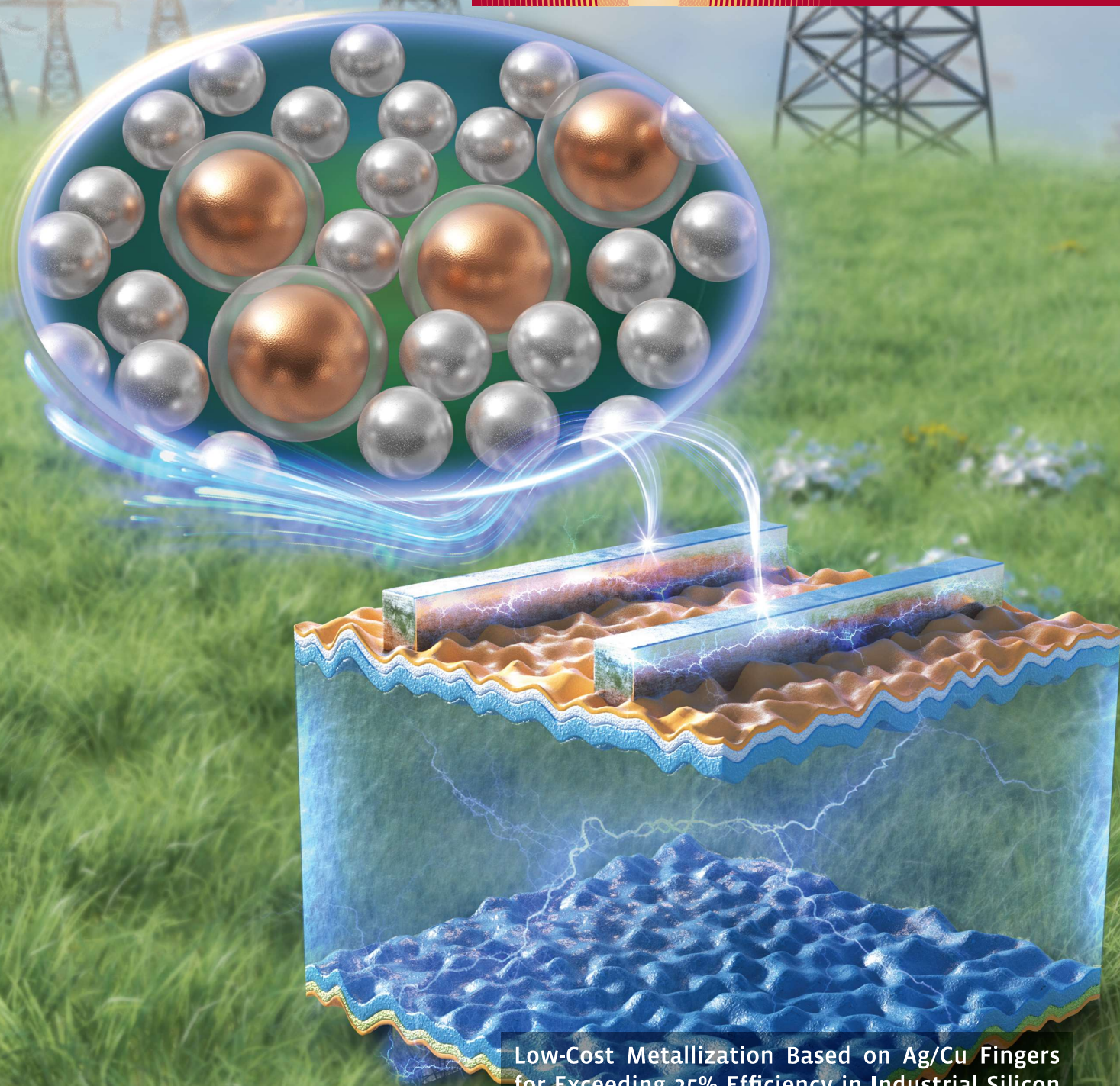
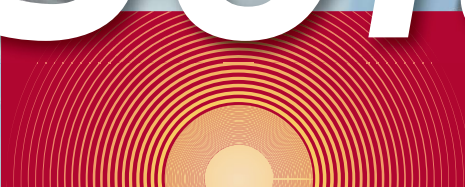


www.solar-rrl.com

ISSN 2367-198X · Sol. RRL · 8 · No. 12 (2024)

12/2024

# Solar RRL



Low-Cost Metallization Based on Ag/Cu Fingers  
for Exceeding 25% Efficiency in Industrial Silicon  
Heterojunction Solar Cells

Wenzhong Shen and co-workers

WILEY-VCH



# Low-Cost Metallization Based on Ag/Cu Fingers for Exceeding 25% Efficiency in Industrial Silicon Heterojunction Solar Cells

Daxue Du, Huanpei Huang, Xingbing Li, Sheng Ma, Dongming Zhao, Rui Li, Haiwei Huang, Zhidan Hao, Fanying Meng, Lin Li, Li He, Dong Ding, Zhengxin Liu, Wenbin Zhang, and Wenzhong Shen\*

Although Ag-coated Cu technology is considered to be an effective approach to mitigate the metallization expenses associated with silicon heterojunction (SHJ) solar cells, there is limited reporting on the photovoltaic performance and reliability of devices employing Ag/Cu electrodes. Herein, industrial SHJ solar cells were successfully fabricated, yielding an average efficiency of 25.18% with bifacial Ag/Cu fingers, which caused a 0.13% decline in efficiency but saved 46% in Ag consumption when compared to traditional Ag fingers. Performance degradation is demonstrated to originate essentially from the front rather than rear Ag/Cu fingers, as revealed by a comprehensive analysis of resistances enhancement and optical losses. Notably, the Ag/Cu fingers exhibited 1.4% lower printed qualification rate and similar high-temperature stabilities in contrast to Ag fingers. In the results, valuable insights were provided for further optimization of low-cost and high-efficiency SHJ solar cells based on Ag/Cu electrodes.

## 1. Introduction

As the potential of the passivated emitter and rear cell is exhausted, the widespread adoption of tunneling oxide passivation contact (TOPCon) solar cells is attributed to the ability to upgrade the manufacturing process on existing production lines.<sup>[1,2]</sup> Compared with TOPCon, silicon heterojunction (SHJ) technology possesses the advantages of simple processes, superior passivation, higher bifaciality, lower degradation, and silicon consumption, etc.,<sup>[3–6]</sup> which is attracting growing interest. Moreover, SHJ solar cells have achieved remarkable efficiency records, reaching 26.8% for the single-junction cell<sup>[7]</sup> and 33.9% for the perovskite/silicon tandem solar cell.<sup>[8]</sup> Hence, according to the latest International Technology Roadmap for

Photovoltaic (ITRPV, 2023), SHJ solar cells are projected to capture a 25% market share by 2030.<sup>[9]</sup> Nevertheless, the current high costs pose a significant impediment to the development of SHJ solar cells.<sup>[10,11]</sup>

One of the biggest challenges of SHJ technology is the metallization cost, constituting over 50% of the expenses in non-silicon materials.<sup>[11]</sup> Due to the temperature tolerance of transparent conductive oxides (TCOs) and hydrogenated amorphous silicon (a-Si: H) films,<sup>[12–15]</sup> the metallization temperature of SHJ stays typically below 250 °C,<sup>[16]</sup> much lower than conventional temperature level (>800 °C).<sup>[17]</sup> On one hand, introducing a new low-temperature process boosts the cost of Ag paste.<sup>[18]</sup> On the other hand, since the increase in electrode resistance is caused by low-temperature sintering, a higher Ag consumption has to be accepted to reduce the grid spacing, thereby suppressing the elevated resistance.<sup>[19]</sup> To reduce the metallization cost, replacing Ag with a cheaper metal is considered as a practical solution. Among the various programs to reduce Ag, Cu electroplating<sup>[20]</sup> and Ag/Cu paste<sup>[21]</sup> have gained wide recognition.

Recently, Cao et al.<sup>[22]</sup> achieved a certified efficiency of 26.4% by employing the electroplating method to prepare Cu electrodes on SHJ cells. Despite the commendable photovoltaic performance achieved by Cu electroplating, tedious processes and expensive equipment create significant cost challenges.<sup>[23,24]</sup>


D. Du, H. Huang, S. Ma, L. Li, L. He, D. Ding, W. Shen  
Institute of Solar Energy, and Key Laboratory of Artificial Structures and Quantum Control (Ministry of Education)  
School of Physics and Astronomy  
Shanghai Jiao Tong University  
Shanghai 200240, P. R. China  
E-mail: wzshen@sjtu.edu.cn

D. Du, X. Li, W. Zhang, W. Shen  
Guosheng Energy Research Institute  
Xuzhou 221011, P. R. China

D. Zhao  
Huaneng Clean Energy Research Institute  
Beijing 102200, P. R. China

R. Li, H. Huang, Z. Hao  
Huaneng Gansu Energy Development Co., Ltd.  
Lanzhou 730070, P. R. China

F. Meng, Z. Liu  
Research Center for New Energy Technology  
Shanghai Institute of Microsystem and Information Technology (SIMIT)  
Chinese Academy of Sciences  
Shanghai 200240, P. R. China

 The ORCID identification number(s) for the author(s) of this article can be found under <https://doi.org/10.1002/solr.202400052>.

DOI: 10.1002/solr.202400052

Additionally, electroplating usually raises environmental concerns.<sup>[24]</sup> In contrast, the utilization of Ag-coated Cu paste emerges as a more economical and environmentally friendly alternative, which is attributed to the simplicity of the preparation process and compatibility with existing printing equipment.<sup>[25]</sup> After decades of development, various methods for preparing Ag-coated Cu have been explored, including displacement reaction, spray pyrolysis, chemical reduction, etc.<sup>[26–29]</sup> Although the Ag-coated Cu technology is believed to turn into the mainstream within a few years,<sup>[10]</sup> the impact of Ag/Cu pastes on photovoltaic performance, particularly in industrial SHJ solar cells, remains largely undisclosed. More importantly, there are few reports on the reliability and stability of Ag/Cu electrodes so far, which are the essential prerequisites for practical applications.

In this work, we have investigated the influence of Ag/Cu fingers on the performance of industrial SHJ solar cells through the screen-printing process. The printability of Ag/Cu pastes was assessed through width and height statistics, as well as cross-sectional morphology. Furthermore, the Ag consumption of the printed fingers was estimated by counting the weight and concentration. We systematically analyzed and compared the electrical and optical characteristics with varying Ag/Cu finger designs using Ag fingers as the control sample. Optical simulations were performed to vividly illustrate the wavelength-dependent electric field distribution and quantify the optical losses induced by the Ag/Cu fingers. Finally, the reliability and stability of the Ag/Cu fingers were verified by printed qualification rate and the efficiency change under heat treatment, respectively.

## 2. Experimental Section

### 2.1. Device Fabrication

As depicted in **Figure 1a**, the composition of the SHJ solar cell includes indium tin oxide (ITO)<sub>973</sub>/nc-SiO<sub>x</sub>:H/i-a-Si:H/c-Si/i-a-Si:H/p-a-Si:H/ITO<sub>9010</sub>. Monocrystalline n-type Czochralski silicon wafers measuring 182 × 91 mm were chosen, possessing a thickness of 120 μm and resistivities ranging from 1 to 2 Ω cm. **Figure 1b** exhibits the preparation processes of SHJ cell. Initially, the wafers underwent immersion in KOH and H<sub>2</sub>O<sub>2</sub> solutions to remove stains and etch surface damage. Next, the substrates were textured via anisotropic etching using KOH solutions. After cleaning and drying, a sequential deposition of intrinsic 1) hydrogenated amorphous silicon (a-Si: H) and n-type hydrogenated nanocrystalline silicon oxide (nc-SiO<sub>x</sub>: H) was carried out on the front side by the plasma-enhanced chemical vapor

deposition. Simultaneously, an i/p-type a-Si: H stack was deposited on the opposite side. TCO films (front: In/Sn = 97/3, rear: In/Sn = 90/10) were deposited using the physical vapor deposition method. Lastly, bifacial figures (front: 50, rear: 98) and bus-bars (front: 16, rear: 16) were produced through screen-printing using the same grid template, following the annealing process at 200 °C for 8 min. This study explores the application of Ag/Cu pastes (≈50 wt% Ag) to industrial SHJ solar cells, with Ag paste (≈93 wt% Ag) serving as a comparative reference.

### 2.2. Characterization

The field-emission transmission electron microscope (TEM, FEI Talos F200X G2, USA) was employed to observe the morphology and element distribution mappings of Ag/Cu powders. The thermogravimetric (TG) analysis (TGA8000, PerkinElmer, USA) was employed to observe the thermal stability of the Ag/Cu powers. The Ag and Ag/Cu powers were characterized by X-ray diffraction (XRD, D8 ADVANCE Da Vinci, Bruker). The surface morphology and size of the metal fingers were observed by the Zeta 3D Instruments (Zeta-20, USA) and field-emission scanning electron microscope (SEM, Zeiss Ultra Plus, Germany). The weights of the fingers were measured by a precise electronic balance (JJ224BC, China) with an accuracy of 0.1 mg. The transmission line model (VS6851, China) was used to evaluate volume resistance and contact resistivity for the complete SHJ solar cells. The quantum efficiency measurements system (PVE300-IVT210, Bentham) collected external quantum efficiency (EQE) and reflectance (small spot) spectra in the wavelength range from 300 to 1180 nm. The reflectance (big spot) spectra were measured by UV-vis spectrophotometer (Lamda950, PerkinElmer, USA). Finally, Vision VS-6831S (AAA level) tested the current-voltage (I–V) parameters in the air under standard simulated AM 1.5G sunlight irradiance.

### 2.3. Simulation

The optical performance of the SHJ solar cell was simulated to assess the impact of the front and rear fingers. The Wave Optics Module of COMSOL Multiphysics 5.5<sup>[30,31]</sup> was employed for this simulation. Material types and thicknesses adhered to our experimental work, with the only deviation being the adjustment of the c-Si substrate to 20 μm for reducing the simulation time and highlighting effects obscured by the size disparity between c-Si and other materials. The standard AM 1.5G spectrum acted as the incident light source, and the refractive indexes and

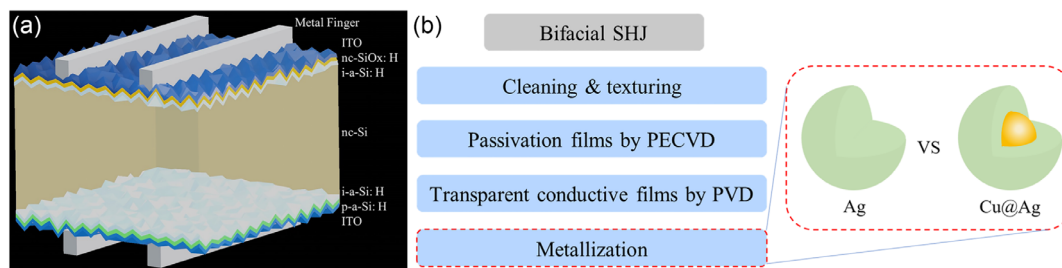


**Figure 1.** a) Schematic structure of the SHJ solar cell. b) The industrial fabricated process for SHJ solar cell.

extinction coefficients of the stacks were sourced from relevant literature.<sup>[32–34]</sup> By solving the system of Maxwell's equations based on the finite-element method, we could obtain the electric field distribution inside the solar cell at a specific wavelength. Furthermore, the online optical simulations were carried out via Wafer Ray Tracer,<sup>[32]</sup> which provided specific results for optical losses, including reflection, transmission, and parasitic absorption.

### 3. Results and Discussion

#### 3.1. Morphology and Properties of Cu@Ag Microspheres

As TEM images displayed in **Figure 2a**, Ag/Cu powder used to print metal fingers on the solar cell comprises two distinct particle sizes: Cu@Ag core-shell microspheres (red arrows) and Ag nanoparticles (blue arrows). **Figure 2b** illustrates a view of Ag nanoparticles, which need to be added to fill the gaps among the Cu@Ag microspheres to ensure a favorable adhesion and conductivity of the printed fingers. Hence, the monodispersity of Ag nanoparticles is not rigidly desired. **Figure 2c–f** presents the high-angle annular dark-field scanning transmission electron micrograph (HAADF–STEM) image of Cu@Ag microspheres, and the corresponding element distribution mappings of Cu@Ag, Cu, and Ag. Evidently, several micrometers of Cu core are uniformly coated by an approximately 200 nm thick Ag layer, maintaining a sharp demarcation. To significantly minimize metallization costs, the size of Cu@Ag microspheres is essentially determined by the Cu core rather than the Ag shell, since Cu much cheaper than Ag.<sup>[18]</sup>

In **Figure 3a**, the XRD spectra reveal diffraction peaks of Ag powder at 38.1°, 44.3°, and 64.4° corresponding to the (111), (200), and (220) crystal planes (JCDs#No.4-783), respectively, while those of Cu are observed at 43.6°, 50.7°, and 74.4° (JCDs#No.4-836). Interestingly, the characteristic peaks of Ag

slightly shift toward a larger angle in Cu@Ag compared to pure Ag, which represents favorable co-lattice growth of Ag along the surface of Cu.<sup>[29]</sup> Notably, no peaks corresponding to CuO or Cu<sub>2</sub>O appear, confirming excellent oxidation resistance at room temperature. To further validate the oxidation effect of Cu@Ag powder at high temperatures, TG tests were carried out in the air from 25 to 700 °C with a temperature increasing rate of 10 °C min<sup>−1</sup>. It can be observed in **Figure 3b** that the weight variation of Ag and Cu@Ag powders basically remains consistent up to 600 °C, where the weight of the Ag powder decreased by 3.5% with increasing temperature due to the organic functional groups and water carried on the surface removed.<sup>[35]</sup> When the temperature exceeds 600 °C, the weight of the Ag powder remains essentially stable, while that of the Ag/Cu powder rises significantly, since the Cu oxidation at a high temperature brings about an additional weight of oxygen. CuO or Cu<sub>2</sub>O suffers from a drastic reduction in conductivity compared to Cu,<sup>[21,36]</sup> indicating Ag/Cu pastes not suitable for solar cells that involve heat treatment above 600 °C. Therefore, Cu@Ag technology is regarded as the key to competing SHJ with TOPCon solar cells.

#### 3.2. Fingers-Printing Effect

Ag and Ag/Cu powders are printed on the front and rear side of the SHJ solar cell after drying at 200 °C for 10 min. The height and width of metal fingers were observed under a Zeta 3D microscope to identify the sizes printed from different pastes in **Figure 4a,b**. Ag/Cu figures have larger widths and more irregular edges than Ag figures, since Cu@Ag microspheres feature inferior printability verified by the SEM cross-sectional images in **Figure 4c,d**. Meanwhile, some distributed voids can be observed inside the Ag/Cu finger, but not inside the Ag finger. Poor finger densification emerges in substandard tension and conductivity, suggesting the need for further adjustment of the particle size gap and organic additives.

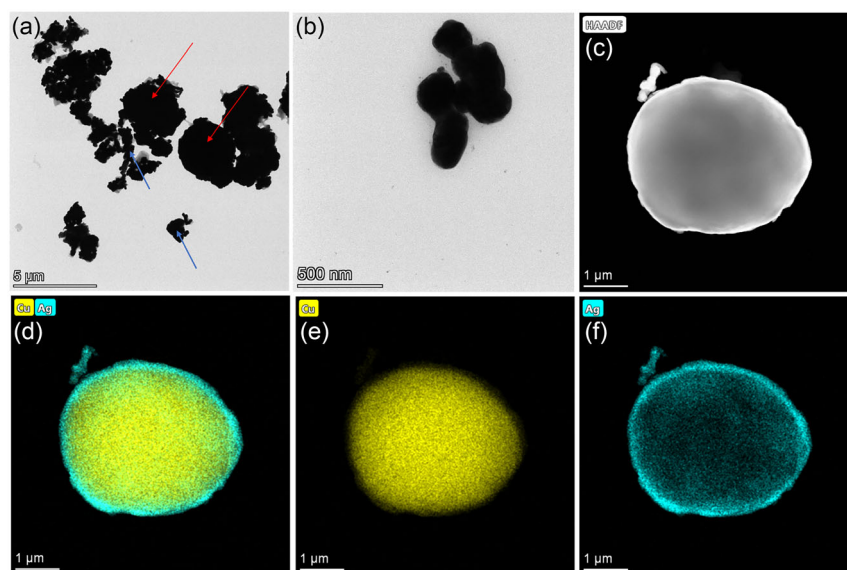


**Figure 2.** a) TEM images of the Ag/Cu powder consisting of Cu@Ag microspheres and Ag nanoparticles, b) TEM images of the Ag nanoparticles, and c) HAADF–STEM image of Cu@Ag core-shell microspheres and corresponding element distribution mapping images of d) Cu@Ag, e) Cu, and f) Ag.



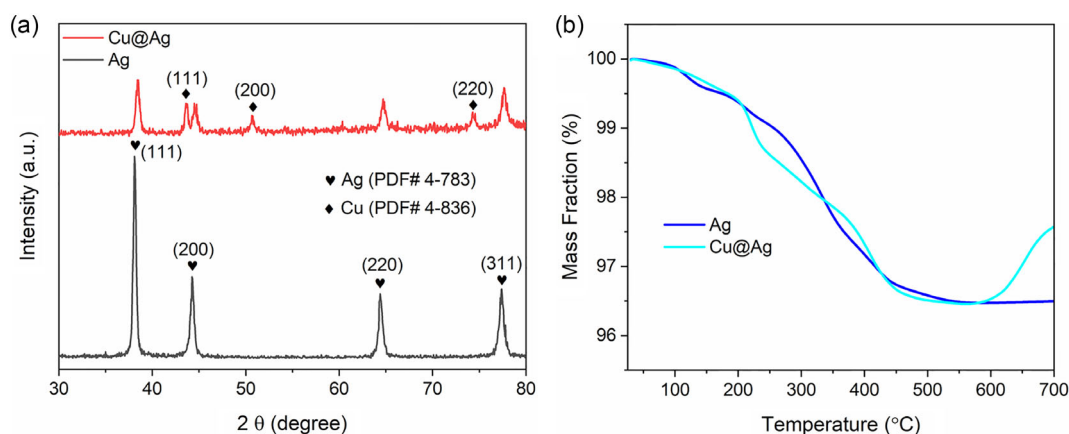


**Figure 3.** a) X-ray diffraction (XRD) patterns and b) thermogravimetric (TG) curves of Ag and Ag/Cu particles used to prepare metal fingers.

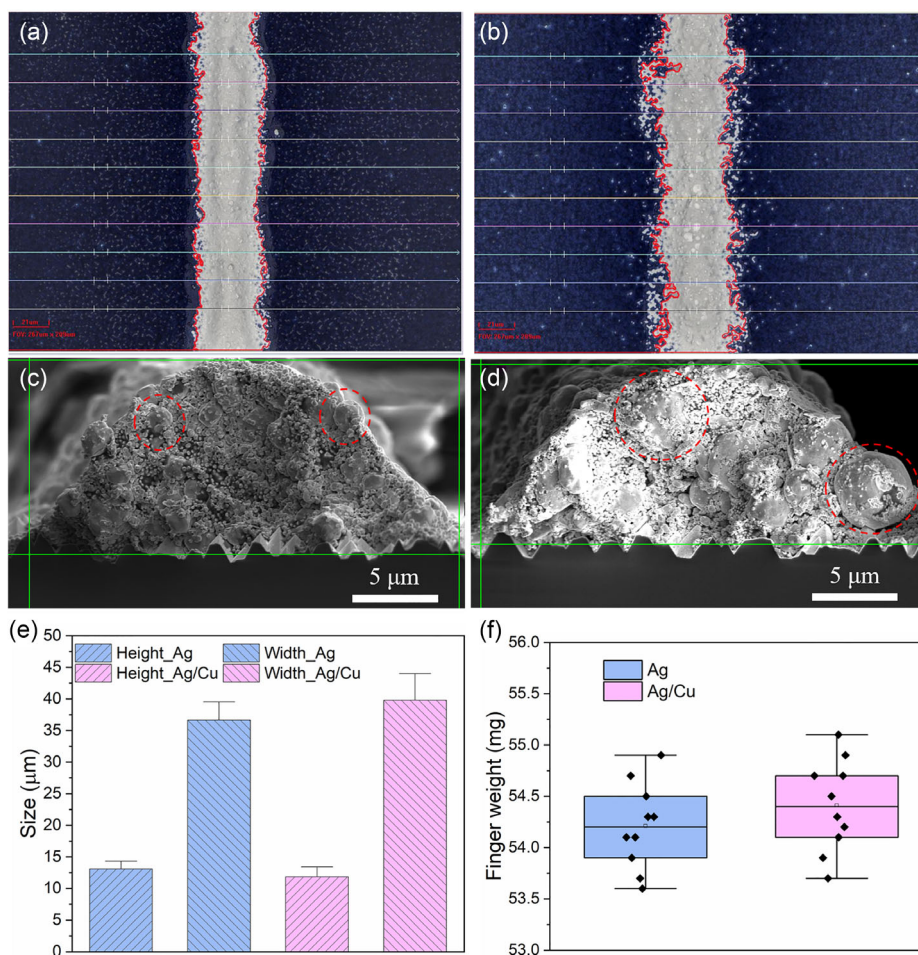


**Figure 4.** a,b) The Zeta top view and c,d) SEM cross-sectional images of Ag and Ag/Cu fingers. e) Height and width statistics based on Ag and Ag/Cu fingers from Zeta 3D microscope. f) Weight statistics based on Ag and Ag/Cu fingers.

As presented in Figure 4e, the average height and width of the fingers were calculated with data from a Zeta 3D microscope, and the detailed parameters are summarized in Table 1. When comparing the Ag fingers with an average height of 13.47 μm and

width of 36.64 μm, a decrease of 0.72 μm in height and an increase of 3.74 μm in width of Ag/Cu fingers result in a worse printability. For the same reason, the Ag/Cu fingers also present a wider distribution in both height and width. To determine the

**Table 1.** The sizes and weights of the metal fingers in SHJ solar cells.

Finger types	Height, $H$ [ $\mu\text{m}$ ]	Width, $W$ [ $\mu\text{m}$ ]	$H/W$	Weight [mg]
Ag	$13.47 \pm 0.61$	$36.64 \pm 2.05$	0.368	54.21
Ag/Cu	$12.75 \pm 1.06$	$40.38 \pm 2.68$	0.316	54.40

Ag consumption, the weight of the bifacial fingers was tested after deducting the mass of the other materials. Interestingly, a similar average weight of  $\approx 54$  mg was obtained on bifacial Ag and Ag/Cu fingers in Figure 4f, which is attributed to the antagonistic effect of a lower density of Cu ( $8.96 \text{ g cm}^{-3}$ ) than Ag ( $10.49 \text{ g cm}^{-3}$ ) and a larger printed volume of Ag/Cu fingers than Ag fingers. Accounting for the Ag content of different pastes, we estimated a 46% savings in Ag consumption using bifacial Ag/Cu fingers.

### 3.3. Electrical and Optical Performance

Annealing treatments commonly facilitate the conductivity of the finger and the contact performance between the metal electrodes and ITO. Due to the narrow selectable range of annealing temperatures for SHJ solar cells,<sup>[37]</sup> we optimized the annealing time to obtain the best performance for the Ag/Cu fingers in Figure 5a. As the annealing time increases from 4 to 10 min, the volume resistance gradually decreases from 5.04 to  $4.84 \Omega \text{ cm}$  accompanied by a drop in the magnitude of the decrease. The contact resistivity showed a similar trend until a minimum of  $1.19 \Omega \text{ cm}^2$  was achieved at 8 min annealing, while the contact resistivity increased instead at 10 min, which is explained by the prolonged heat treatment causing partial escape of hydrogen atoms from the passivation film,<sup>[13]</sup> and thus increasing the contact resistivity of the whole cell system. Therefore, an 8 min annealing time was preferred based on the balance of performance and economy. Furthermore, the resistance profiles of Ag and Ag/Cu fingers were compared under the same annealing conditions. As presented in Figure 5b, the Ag/Cu reveals a contact resistance of  $4.87 \Omega \text{ cm}$ , close to  $4.77 \Omega \text{ cm}$  for the Ag. Considering the boosted resistance by the inside holes, the volume resistance of Ag/Cu fingers has the potential to be even lower than Ag by further optimization. Similarly, Ag/Cu fingers demonstrate a slightly higher contact resistivity ( $0.04 \Omega \text{ cm}^2$ ) between ITO and metal fingers than Ag fingers.

Metal fingers not only serve the electrical function of transmitting current but also exert a fundamental influence on the optical absorption of the solar cell. To compare how the finger affects the bifacial SHJ solar cells under front illumination, EQE spectra and reflectance were measured with different fingers in a wavelength range of 300–1180 nm. As inserted in Figure 6a illuminated by a small light spot between the two adjacent fingers, the EQE of SHJ solar cells with bifacial Ag and Ag/Cu fingers exhibit robust wavelength-dependent differences, which is consistent with the evidence of reflectance in Figure 6b. First, reflectance values in the 300–650 nm are uniform for the four different finger designs, since the reflection is mainly determined by the front surface, when the incident light cannot reach SHJ solar cell the bottom based on the large extinction coefficient of Si (Figure S1, Supporting Information). The front films (including ITO, nc-SiOx:H, and i-a-Si:H) have strong parasitic absorption at 300–650 nm but not in the longer wavelength section,<sup>[33]</sup> leading to the escaped photons inside the cell can contact the front fingers. As the electric field intensity at 700 nm shown in Figure 6c, the incident light does not reach the bottom but is concentrated on the front surface. Accordingly, bifacial Ag/Cu fingers get a slightly lower reflection at 650–1030 nm than bifacial Ag fingers provided by the front Ag/Cu fingers, owing to that a wider front finger can block more escaping photons. However, due to the sharp attenuation of the Si extinction coefficient with the wavelength growing, incident photons with long wavelengths can reach the cell bottom, where more photons arrive at a larger wavelength. Figure 6d offers visual evidence of the significant boosting of the rear metal layer (RML) on the electric field intensity (i.e., absorption intensity) of SHJ solar cells at 1100 nm. Hence, a wider rear electrode reflects more photons from the bottom, and thus partial photons pass through the cell in reverse increasing the reflection. Significantly, the EQE enhancement of bifacial Ag/Cu fingers during 1030–1180 nm contributes to the rear side.

To quantify the optical loss caused by the rear fingers, we performed an optical simulation via Wafer Ray Tracer software, as shown in Figure 6e. It can be found that the optical energy loss of the SHJ solar cell amounts 15.05% without the RML and 11.92% with the RML. The difference stems from the fact that the RML blocks the photons with long wavelengths at the cell bottom originally categorized as the transmitted part. This 8.11% of the transmitted energy is roughly converted into three parts: 2.45% of escaped reflection, 2.36% of rear film absorptions,

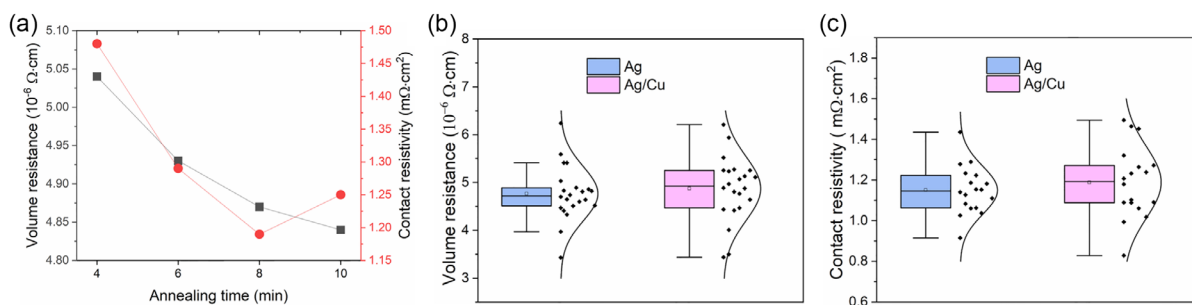


**Figure 5.** a,b) Effect of annealing time on volume resistance and contact resistivity of fingers. Statistical distribution of (b) volume resistance and (c) contact resistivity based on Ag and Ag/Cu fingers with 8 min annealing.

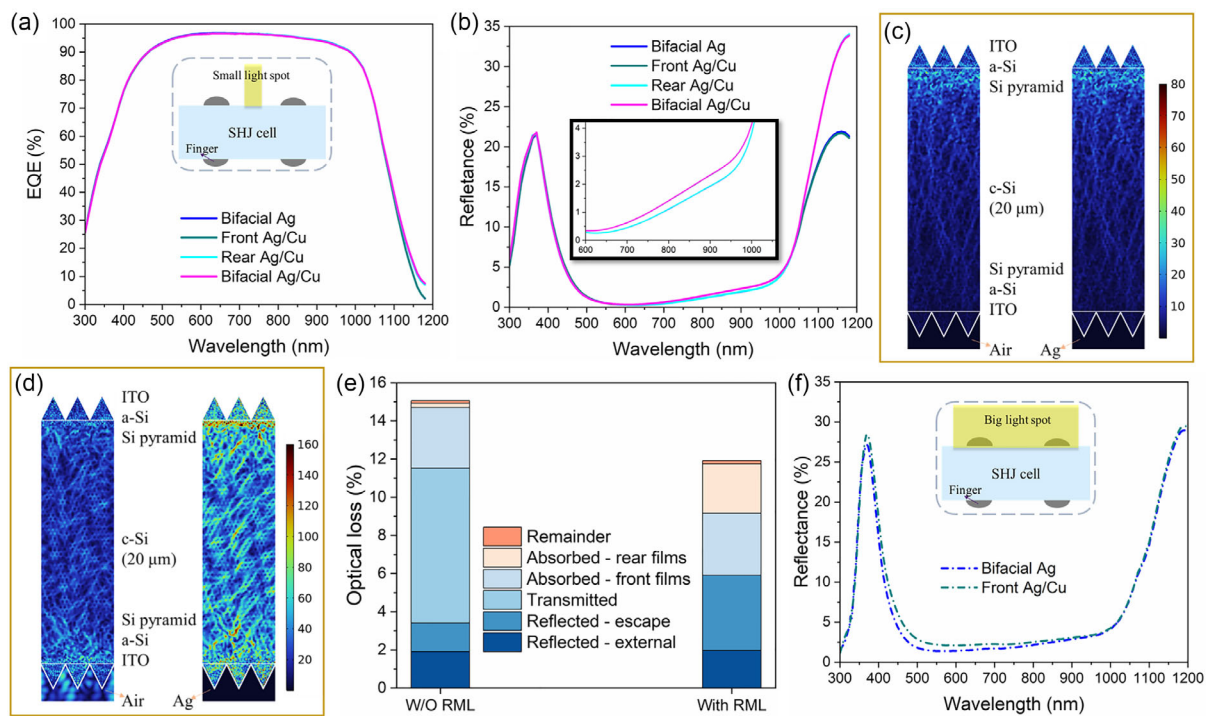


**Figure 6.** a) EQE and b) reflectance of SHJ solar cells with a small light spot for the four different finger designs. Electric field intensity distribution of SHJ solar cells without and with rear metal layer (RML) at c) 700 nm and d) 1100 nm. e) Optical loss of SHJ solar cells without and with RML and f) reflectance of SHJ solar cells with a big light spot for the two different finger designs.

and 3.13% of c-Si absorption. Therefore, widening the rear electrodes facilitates the enhancement of light absorption, which is particularly essential for the future thinning of SHJ solar cells.<sup>[6,38]</sup> The reflection performance for the front fingers was also compared when illuminated by a big light spot with a diameter of  $>2$  cm, as illustrated in Figure 6f. Compared to bifacial Ag fingers, the front Ag/Cu ones maintain a reflection improvement within 0.5% across the entire operating waveband, except near 500 nm, where the anomalous reflectance rising is assumed to be the shape effect<sup>[30,39]</sup> because of Ag/Cu fingers featuring a smaller aspect ratio. Consequently, the shape effect also deserves to be emphasized rather than just the width when designing the front fingers of a solar cell.

### 3.4. Current Density–Voltage Parameters

The position of the Ag/Cu fingers affects the optical and electrical properties of the SHJ solar cell. Hence, we depicted the normalized statistical current density–voltage ( $J$ – $V$ ) parameters on three different Ag/Cu finger arrangements with the Ag fingers as a baseline, and the parameters are summarized in Table 2. As shown in Figure 7a, the front Ag/Cu fingers cause a  $0.17 \text{ mA cm}^{-2}$  loss in short-circuit current density ( $J_{\text{SC}}$ ) while the rear ones provide a  $0.10 \text{ mA cm}^{-2}$  gain, which is consistent with Figure 6. As a result, the SHJ solar cell only obtained a  $J_{\text{SC}}$  loss of  $0.07 \text{ mA cm}^{-2}$  due to the application of bifacial Ag/Cu fingers in place of Ag fingers. Nevertheless, the open-circuit voltage ( $V_{\text{OC}}$ ) was observed to be reduced by about 0.5 mV in Figure 7b regardless of whether front or rear Ag/Cu fingers were

**Table 2.** Photovoltaic performance of SHJ solar cell with Ag and Ag/Cu fingers.

	$J_{\text{SC}}$ [ $\text{mA cm}^{-2}$ ]	$V_{\text{OC}}$ [mV]	FF [%]	PCE [%]	$R_{\text{s}}$ [ $\text{m}\Omega$ ]
Bifacial Ag	0	0	0	0	0
Rear Ag/Cu	+0.10	−0.5	−0.12	−0.01	+0.11
Front Ag/Cu	−0.18	−0.6	−0.21	−0.13	+0.19
Bifacial Ag/Cu	−0.08	−1.0	−0.29	−0.13	+0.27

used, which originated from a mismatch in the work functions<sup>[40]</sup> between the finger and the ITO justified by the elevated contact resistivity in Figure 5c. Although the  $V_{\text{OC}}$  reduction is insignificant (1.1 mV), the pursuit of a higher  $V_{\text{OC}}$  with bifacial Ag/Cu fingers can be achieved by modulating the ITO or metal paste.

Meanwhile, the fill factor (FF) of the SHJ solar cells also decreased by 0.12% in the front side and 0.21% in the rear side in Figure 7c, which correlates with the increase in series resistance ( $R_{\text{s}}$ ). Figure 7d illustrates the front and rear  $R_{\text{s}}$  improve by 0.11 and 0.19  $\text{m}\Omega$ , respectively, brought by finger resistance and contact resistance. The improvement in  $R_{\text{s}}$  on the rear side is about twice as much as on the front side, since the number of fingers on the back side ( $\times 92$ ) far exceeds that on the front side ( $\times 50$ ) for a balance of optical and electrical properties. Based on the results of  $J_{\text{SC}}$ ,  $V_{\text{OC}}$ , and FF, a similar average power conversion efficiency (PCE) can also be obtained using rear Ag/Cu fingers compared to bifacial Ag/Cu fingers in Figure 7e.



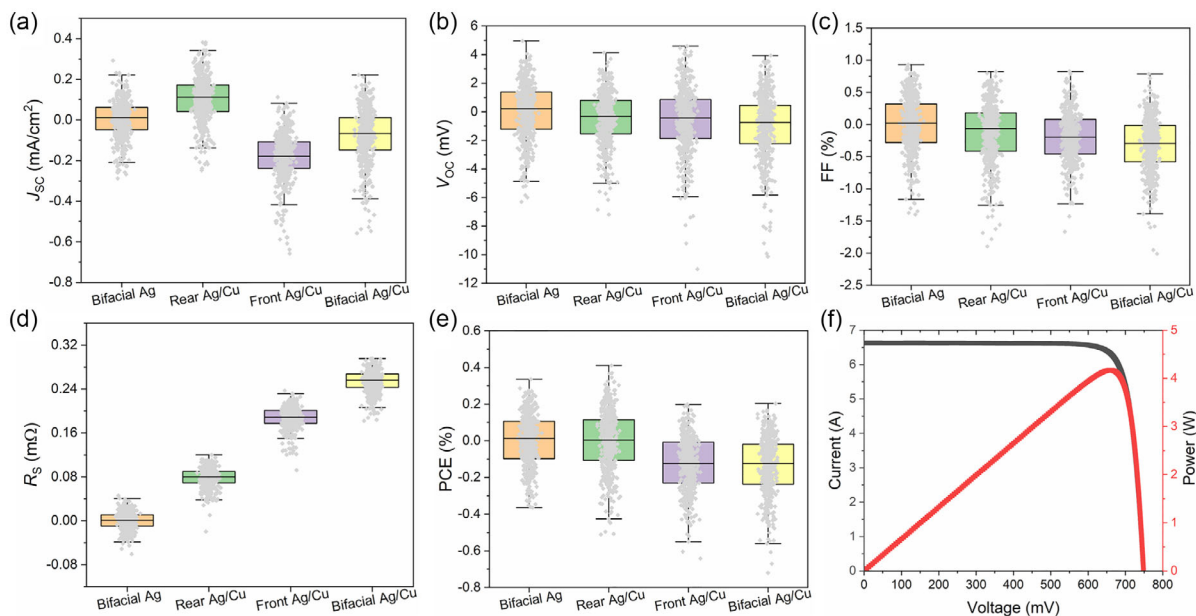


**Figure 7.** Measured  $J-V$  parameters (>500 samples per group) of the SHJ solar cells with Ag and Ag/Cu fingers, including a)  $J_{sc}$ , b)  $V_{oc}$ , c) FF, d)  $R_s$ , and e) PCE. f) Representative  $I-V$  and  $P-V$  curves of the fabricated SHJ solar cells with bifacial Ag/Cu fingers.

Therefore, 0.13% of the PCE loss mainly derives from the front side. Figure 7f provides representative  $I-V$  and power-voltage ( $P-V$ ) curves of the SHJ solar cell with bifacial Ag/Cu fingers, achieving the average PCE of 25.18% and power of 4.17 W.

### 3.5. Fingers Reliability and Stability

The reliability and stability of Ag/Cu fingers are worthy of attention, which is the premise of mass production. The reliability of the finger appearance is quickly distinguished by a high-definition

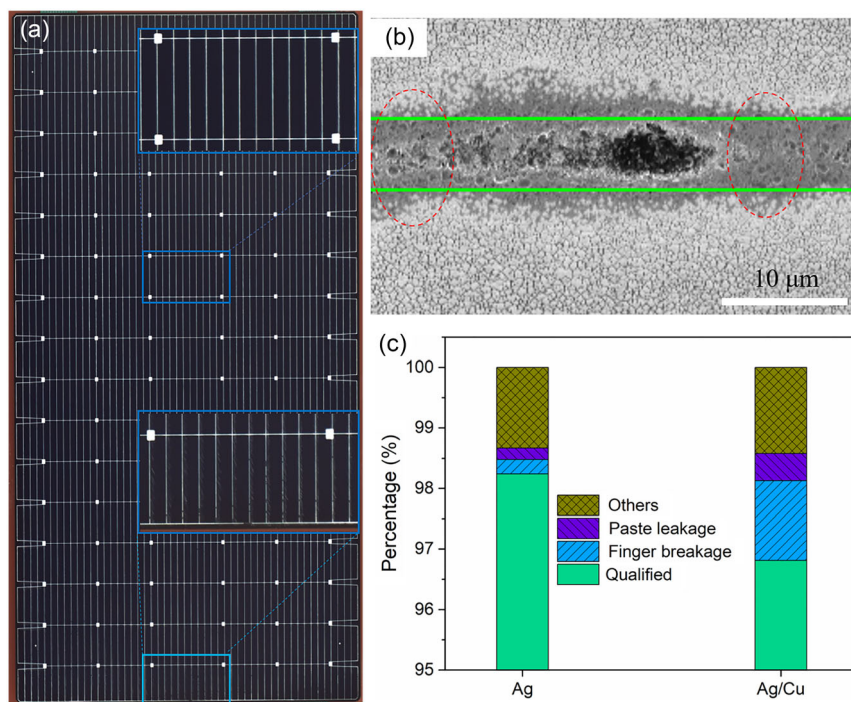


**Figure 8.** a) Front photograph of the SHJ solar cell with the localized enlargements of Ag/Cu fingers at the center and edge. b) SEM image of a broken Ag/Cu finger. c) Statistics on the qualification rate of the SHJ solar cell with Ag and Ag/Cu fingers.



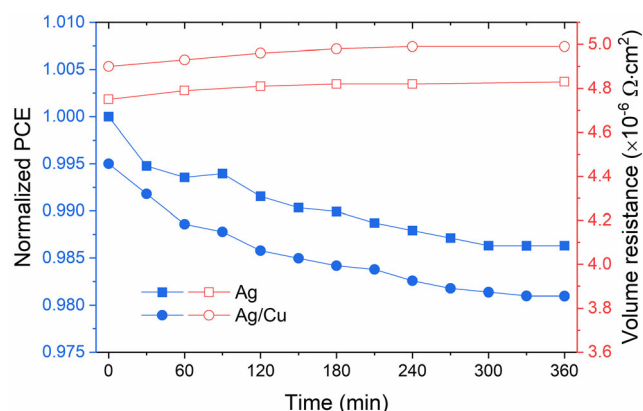


**Figure 9.** Normalized PCE and volume resistance of the SHJ solar cell with bifacial Ag and Ag/Cu fingers versus treatment time at 150 °C.

camera. **Figure 8a** illustrates a typical front photograph of a SHJ solar cell with broken Ag/Cu fingers. Based on the enlarged view of the middle and edge positions, it can be found that the broken fingers occur mainly at the edge position rather than the middle position. Furthermore, the microstructure of the fracture is clearly presented by SEM image in **Figure 8b**. Oversized Cu@Ag microspheres result in less paste distribution at the cell edges, and the agglomeration of the microspheres leaves nearby locations unprinted (red circles). Although the PCE loss induced by finger breakage can be controlled within a manageable range through the design of multiple fingers, **Figure S2** Supporting Information, exhibits device performance for broken fingers with an average PCE decay of 1.1% based on an industrial screen-printing process. However, the life degradation of the PV module and the hot spot effect with broken fingers can hardly be avoided under outdoor conditions.<sup>[41,42]</sup> As shown in **Figure 8c**, we counted the qualification rate of the grid appearance from more than 500 samples in each group, reaching 98.24% and 96.81% for Ag and Ag/Cu fingers, respectively. The shortfall derives mainly from finger breakage which contributes 1.43%, followed by 0.26% of paste leakage (**Figure 8**).

Additionally, to check the long-term stability of Ag/Cu fingers under high temperatures, SHJ solar cells were heat treated in an air environment at 150 °C to verify the pitfalls for oxidation-induced attenuation of fingers. Since 150 °C is much higher than the maximum operating temperature (<60 °C) of the SHJ solar cells,<sup>[43]</sup> we can achieve accelerated aging results. **Figure 9** demonstrates that the PCE of 25.12% with the bifacial Ag fingers decreases by 1.4% after 6 h of heat treatment, and the Ag/Cu fingers depict a similar effect, with the normalized PCE decreasing from 0.995 (24.99%) to 0.981 (24.64%). In addition, the enhancement of volume resistance is also controlled within 0.1  $\Omega \cdot \text{cm}$  after heat treatment of fingers. The superior reliability of Ag/Cu fingers (50 wt% Ag) was proved by almost no extra attenuation because of the favorable antioxidation property of Ag-coated Cu, which is consistent with **Figure 3b**.

## 4. Conclusions

In summary, we have fabricated industrial SHJ solar cells with Ag/Cu fingers utilizing Ag fingers as a control group. The Ag/Cu

powders demonstrate effective antioxidation up to 600 °C, attributed to the well-coated Cu core with an Ag layer. An annealing time of 8 min in the preparation of Ag/Cu fingers was preferred considering the balance between resistance and energy consumption. Owing to the presence of numerous micron-sized Cu/Ag core-shell microspheres, the Ag/Cu fingers exhibit a broader and lower cross-section compared to the Ag fingers. The Ag/Cu fingers caused a weak elevation of volume resistance and contact resistivity, which led to a decrease in  $V_{OC}$  and FF. Nevertheless, the front and rear Ag/Cu fingers were revealed to exert opposite effects on the  $J_{SC}$ . Finally, ultimately, we achieved an average PCE of 25.18% in SHJ solar cells using bifacial Ag/Cu fingers, indicating a marginal 0.13% decrease in PCE but a significant 46% reduction in Ag consumption compared to Ag fingers. Importantly, the qualification rate of Ag/Cu fingers decreased from 98.24% to 96.81%, primarily due to finger breakage. Furthermore, the Ag/Cu fingers passed the challenge of heat treatment at 150 °C for 360 min without inducing performance degradation compared to Ag fingers.

## Supporting Information

Supporting Information is available from the Wiley Online Library or from the author.

## Acknowledgements

This work was supported by the Major State Basic Research Development Program of China (grant no. 2022YFB4200101), the National Natural Science Foundation of China (grant nos. 11974242 and 11834011), Inner Mongolia Science and Technology Project (grant no. 2022JBG0036), and Huaneng Science and Technology Project (grant no. HNKJ22-H154).

## Conflict of Interest

The authors declare no conflict of interest.

## Data Availability Statement

The data that support the findings of this study are available from the corresponding author upon reasonable request.

## Keywords

Ag/Cu fingers, optical losses, resistances, silicon heterojunction (SHJ) solar cells, stabilities

Received: January 21, 2024  
Revised: February 28, 2024  
Published online: March 22, 2024

- [1] B. Kafle, B. S. Goraya, S. Mack, F. Feldmann, S. Nold, J. Rentsch, *Sol. Energy Mater. Sol. Cells* **2021**, 227, 111100.
- [2] W. Shen, Y. Zhao, F. Liu, *Front. Energy* **2024**, 18, 8.
- [3] W. Liu, J. Shi, L. Zhang, A. Han, S. Huang, X. Li, J. Peng, Y. Yang, Y. Gao, J. Yu, K. Jiang, X. Yang, Z. Li, W. Zhao, J. Du, X. Song, J. Yin, J. Wang, Y. Yu, Q. Shi, Z. Ma, H. Zhang, J. Ling, L. Xu,

- J. Kang, F. Xu, J. Liu, H. Liu, Y. Xie, F. Meng, et al., *Nat. Energy* **2022**, 7, 427.
- [4] A. Richter, R. Müller, J. Benick, F. Feldmann, B. Steinhäuser, C. Reichel, A. Fell, M. Bivour, M. Hermle, S. W. Glunz, *Nat. Energy* **2021**, 6, 429.
- [5] J. Yu, P. S. Leonard, D. Qiu, Y. Zhao, A. Lambertz, C. Zahren, L. Volker, W. Duan, J. Yu, K. Ding, *Sol. Energy Mater. Sol. Cells* **2022**, 235, 111459.
- [6] W. Liu, Y. Liu, Z. Yang, C. Xu, X. Li, S. Huang, J. Shi, J. Du, A. Han, Y. Yang, G. Xu, J. Yu, J. Ling, J. Peng, L. Yu, B. Ding, Y. Gao, K. Jiang, Z. Li, Y. Yang, Z. Li, S. Lan, H. Fu, B. Fan, Y. Fu, W. He, F. Li, X. Song, Y. Zhou, Q. Shi, et al., *Nature* **2023**, 617, 717.
- [7] H. Lin, M. Yang, X. Ru, G. Wang, S. Yin, F. Peng, C. Hong, M. Qu, J. Lu, L. Fang, C. Han, P. Procel, O. Isabella, P. Gao, Z. Li, X. Xu, *Nat. Energy* **2023**, 8, 789.
- [8] M. A. Green, E. D. Dunlop, M. Yoshita, N. Kopidakis, K. Bothe, G. Siefer, X. Hao, *Prog. Photovoltaics* **2023**, 32, 3.
- [9] International Technology Roadmap for Photovoltaic, <https://itpvdma.org> (accessed: December 2023).
- [10] China PV Industry Development Roadmap, <http://www.chinapv.org.cn> (accessed: December 2023).
- [11] Z. Sun, X. Chen, Y. He, J. Li, J. Wang, H. Yan, Y. Zhang, *Adv. Energy Mater.* **2022**, 12, 2200015.
- [12] M. Gulen, G. Yildirim, S. Bal, A. Varilci, I. Belenli, M. Oz, *J. Mater. Sci.: Mater. Electron.* **2012**, 24, 467.
- [13] M. Wang, G. Wang, W. Gong, S. Cheng, L. Zhao, X. Xu, D. Gong, F. Ye, L. Mo, H. Diao, W. Wang, *Sol. Energy Mater. Sol. Cells* **2023**, 253, 112229.
- [14] S. D. Wolf, K. Michio, *J. Appl. Phys.* **2009**, 105, 103707.
- [15] Y. Zhao, P. Procel, A. Smets, L. Mazzarella, C. Han, G. Yang, L. Cao, Z. Yao, A. Weeber, M. Zeman, O. Isabella, *Prog. Photovoltaics* **2022**, 31, 1170.
- [16] D. Chen, L. Zhao, H. Diao, W. Zhang, G. Wang, W. Wang, *J. Alloys Compd.* **2015**, 618, 357.
- [17] W. Wu, Z. Zhang, F. Zheng, W. Lin, Z. Liang, H. Shen, *Prog. Photovoltaics* **2018**, 26, 752.
- [18] A. Razzaq, T. G. Allen, W. Liu, Z. Liu, S. De Wolf, *Joule* **2022**, 6, 514.
- [19] M. Taguchi, A. Yano, S. Tohoda, K. Matsuyama, Y. Nakamura, T. Nishiwaki, K. Fujita, E. Maruyama, *IEEE J. Photovoltaics* **2014**, 4, 96.
- [20] J. Geissbühler, S. D. Wolf, A. Faes, N. Badel, Q. Jeangros, A. Tomasi, L. Barraud, A. Descoedres, M. Despeisse, C. Ballif, *IEEE J. Photovoltaics* **2014**, 4, 1055.
- [21] Y. Zeng, C.-W. Peng, W. Hong, S. Wang, C. Yu, S. Zou, X. Su, *Trans. Tianjin Univ.* **2022**, 28, 358.
- [22] C. Yu, K. Gao, C.-W. Peng, C. He, S. Wang, W. Shi, V. Allen, J. Zhang, D. Wang, G. Tian, Y. Zhang, W. Jia, Y. Song, Y. Hu, J. Colwell, C. Xing, Q. Ma, H. Wu, L. Guo, G. Dong, H. Jiang, H. Wu, X. Wang, D. Xu, K. Li, J. Peng, W. Liu, D. Chen, A. Lennon, X. Cao, et al., *Nat. Energy* **2023**, 8, 1375.
- [23] T. Hatt, S. Kluska, M. Yamin, J. Bartsch, M. Glatthaar, *Sol. RRL* **2019**, 3, 1900006.
- [24] J. Yu, J. Li, Y. Zhao, A. Lambertz, T. Chen, W. Duan, W. Liu, X. Yang, Y. Huang, K. Ding, *Sol. Energy Mater. Sol. Cells* **2021**, 224, 110993.
- [25] W. Wang, *Presented at the 34th Inter. Photovoltaic Science and Engineering Conf.*, Shenzhen, China November **2023**.
- [26] Y.-S. Park, C. Y. An, P. K. Kannan, N. Seo, K. Zhuo, T. K. Yoo, C.-H. Chung, *Appl. Surf. Sci.* **2016**, 389, 865.
- [27] D. S. Jung, H. M. Lee, Y. C. Kang, S. B. Park, *J. Colloid Interface Sci.* **2011**, 364, 574.
- [28] O. Güler, T. Varol, Ü. Alver, A. Çanakçı, *J. Alloys Compd.* **2019**, 782, 679.
- [29] Y. Zeng, S. Zou, Z. Chen, Z. Lu, M. Ni, C.-W. Peng, Z. Wang, H. Sun, X. Zhang, X. Su, *J. Mater. Chem. A* **2024**, 12, 1551.
- [30] D. Du, Z. Xu, L. Wang, Y. Guo, S. Liu, T. Yu, C. Wang, F. Wang, H. Wang, *Sol. Energy* **2021**, 224, 10.
- [31] D. Du, F. Qiao, Y. Guo, F. Wang, L. Wang, C. Gao, D. Zhang, J. Liang, Z. Xu, W. Shen, H. Wang, *Sol. Energy* **2022**, 245, 146.
- [32] <https://www.pvlighthouse.com.au> (accessed: December 2023).
- [33] Z. C. Holman, A. Descoedres, L. Barraud, F. Z. Fernandez, J. P. Seif, S. D. Wolf, C. Ballif, *IEEE J. Photovoltaics* **2012**, 2, 7.
- [34] Z. C. Holman, M. Filipič, A. Descoedres, S. D. Wolf, F. Smole, M. Topič, C. Ballif, *J. Appl. Phys.* **2013**, 113, 013107.
- [35] M. Wu, B. Lin, Y. Cao, J. Song, Y. Sun, H. Yang, X. Zhang, *J. Mater. Sci.: Mater. Electron.* **2013**, 24, 4913.
- [36] S. Jeong, K. Woo, D. Kim, S. Lim, J. S. Kim, H. Shin, Y. Xia, J. Moon, *Adv. Funct. Mater.* **2008**, 18, 679.
- [37] W. Duan, G. Mains, H. T. Gebrewold, K. Bittkau, A. Lambertz, B. Xu, V. Lauterbach, A. Eberst, N. Nicholson, L. Korte, M. A. Yaqin, K. Zhang, Q. Yang, U. Rau, K. Ding, *Adv. Funct. Mater.* **2023**, 34, 2310552.
- [38] R. Zhu, Z. Zhang, Y. Li, *Nanotechnol. Rev.* **2019**, 8, 452.
- [39] M. F. Stuckings, A. W. Blakers, *Sol. Energy Mater. Sol. Cells* **1999**, 59, 233.
- [40] J. Zhu, X. Yang, Z. Yang, D. Wang, P. Gao, J. Ye, *Adv. Funct. Mater.* **2018**, 28, 1705425.
- [41] J. Wong, V. Shanmugam, J. Cunnusamy, M. Zahn, A. Zhou, R. Yang, X. Chen, A. G. Aberle, T. Mueller, *Prog. Photovoltaics* **2015**, 23, 1877.
- [42] P. Chaturvedi, B. Hoex, T. M. Walsh, *Sol. Energy Mater. Sol. Cells* **2013**, 108, 78.
- [43] A. Abdallah, D. Martinez, B. Figgis, O. El Daif, *Renewable Energy* **2016**, 97, 860.